Three-dimensional Configuration of Induced Magnetic Fields around Mars

Chi Zhang[1,2,3], Zhaojin Rong[1,2,4], Lucy Klinger[5], Hans Nilsson[3], Zhen Shi[1,2], Fei He[1,2], Jiawei Gao[1,2], Xinzhou Li[1,2], Yoshifumi Futaana[3], Robin Ramstad[6], Xiaodong Wang[3], Mats Holmström[3], Stats Barabash[3], Kai Fan[1,2], and Yong Wei[1,2,4]

[1]Key Laboratory of Earth and Planetary Physics, Institute of Geology and Geophysics, Chinese Academy of Sciences, Beijing, China

[2]College of Earth and Planetary Sciences, University of Chinese Academy of Sciences, Beijing, China

[3]Swedish Institute of Space Physics, Kiruna, Sweden

[4]Mohe Observatory of Geophysics, Beijing National Observatory of Space Environment, Institute of Geology and Geophysics, Chinese Academy of Sciences, Beijing, China

[5]Beijing International Center for Mathematical Research, Peking University, Beijing, China

[6]Laboratory for Atmospheric and Space Physics, University of Colorado, Boulder, CO, USA

***Corresponding author**: Zhaojin Rong (rongzhaojin@mail.iggcas.ac.cn)

Key Points:

- The magnetic field structure has an evident hemispheric asymmetry along the direction of the solar wind electric field.
- The tail current sheet is thicker and has a stronger tailward J×B force near the flank of the +E-hemisphere.
- The effects of IMF Bx, the dynamic pressure of solar wind, and the rotation of the planet on the field structure are surveyed respectively.

Abstract

Using over 6 years of magnetic field data (2014.10-2020.12) collected by the Mars Atmosphere and Volatile EvolutioN (MAVEN), we conduct a statistical study on the three-dimensional average magnetic field structure around Mars. We find that this magnetic field structure conforms to the pattern typical of an induced magnetosphere, that is, the interplanetary magnetic field (IMF) which is carried by the solar wind and which drapes, piles up, slips around the planet, and eventually forms a tail in the wake. The draped field lines from both hemispheres along the direction of the solar wind electric field (**E**) are directed towards the nightside magnetic equatorial plane, which looks like they are "sinking" toward the wake. These "sinking" field lines from the +E-hemisphere (**E** pointing away from the plane) are more flared and dominant in the tail, while the field lines from the –E-hemisphere (**E** pointing towards) are more stretched and "pinched" towards the plasma sheet. Such highly "pinched" field lines even form a loop over the pole of the –E-hemisphere. The tail current sheet also shows an E-asymmetry: the sheet is thicker with a stronger tailward J×B force at +E-flank, but much thinner and with a weaker J×B (even turns sunward) at –E-flank. Additionally, we find that IMF B_x can induce a kink-like field structure at the boundary layer; the field strength is globally enhanced and the field lines flare less during high dynamic pressure; however, the rotation of the planet, against expectations, modulate the configuration of the tail current sheet insignificantly.

Plain Language Summary

To clarify the global magnetic field structure around Mars, we comprehensively study the three-dimensional (3D) magnetic field structure of the Martian magnetosphere based on measurements from MAVEN. Our study derives 3D distribution features of the magnetic field structure, quantitatively estimates the tail current sheet and also investigates possible effects brought by the IMF Bx, the dynamic pressure of solar wind, and planetary rotation on the magnetic field structure. This 3D magnetic field structure around Mars is essential to understanding the dynamic processes of the Martian magnetosphere.

1 Introduction

It is well known that both Venus and Mars lack a global dipole field and that the solar wind plasma flow along with the "frozen-in" interplanetary magnetic field (IMF) interacts with the atmosphere/ionosphere of the planet directly, resulting in an induced magnetosphere. On the dayside, IMF piles up to form a magnetic barrier and drapes around the planet. The draped IMF is stretched by the solar wind and slips into the wake to form an elongated induced magnetotail [e.g., Acuña et al., 1998; Luhmann al., 2004; Ma et al., 2002; McComas et al., 1986]. Researchers realize that most of the planetary ions escape to interplanetary space via the electromagnetic force, e.g. the solar wind electric fields (**E**), the hall electric fields, and the ambipolar electric fields [e.g., Barabash et al., 2007; Dubinin et al., 2011; Lundin, 2011; Dubinin & Fraenz, 2015; Fang et al., 2010; Futaana et al., 2017; Nilsson et al., 2021; Zhang et al., 2021]; therefore, knowledge of the magnetic field structure around the Mars is vital for understanding associated magnetospheric processes (e.g., the escape of planetary ions).

Venus is an ideal natural laboratory for studying an induced magnetosphere because the planet has no significant intrinsic field and only relies on its ionosphere as an obstacle to solar wind. Early studies based on the Pioneer Venus Orbiter have found a structure of draped field lines in the distant downstream tail (8-12 Venusian radii) and demonstrated that there is an asymmetrical tail field structure along the direction of the solar wind electric field (E-asymmetry) [Saunders and Russell, 1986; McComas et al., 1986]. Studies based on observations of the Venus Express, the ESA's first mission to Venus [Titov et al., 2006], demonstrated that E-asymmetry had already occurred in the terminator and the near-Venus tail, suggesting that magnetic field lines are likely wrapped more tightly around Venus in the –E-hemisphere (electric field points towards planet) [Zhang et al., 2010; Du et al., 2013]. Rong et al. [2014] reconstructed the three-dimensional (3-D) field structures of the near-Venus tail and found that its draped field lines would sink into the wake, while the magnetic field structure of the tail current sheet would become irregular in the –E-hemisphere. Chai et al. [2016] suggested that a global looping field around the tail might occur in addition to the draped field lines.

Unlike the induced magnetosphere of Venus, Mars has patches of localized intense remnant crustal fields, particularly in the southern hemisphere [e.g., Acuña et al., 1999; Connerney et al., 2005]. These crustal fields contribute to solar wind interactions, complicating the Martian space environment. Although many studies in the past several decades have been conducted based on

the spacecraft missions such as Phobos-2, Mars Global Surveyor, and Mars Express [e.g., Yeroshenko et al., 1990; Halekas et al., 2006; Barabash et al., 2007; Fedorov et al., 2006], our knowledge about the magnetic field structure of Mars' magnetosphere is lacking due to limited orbit coverage and inadequate scientific equipment. However, NASA's recent mission on the Mars Atmosphere and Volatile EvolutioN (MAVEN) spacecraft carried both magnetometer and plasma instruments and provided global coverage of the Martian space environment within 3 R_m (R_m= 3390km, Mars radius), with an orbit period of about 4.5 hours [Jakosky et al. 2015], enabling us to study the global average magnetic field configuration around Mars.

Based on MAVEN observations, Harada et al. [2015] found that the tightly-wrapped field lines and the sunward flow of ionospheric plasma tend to occur in the –E-hemisphere. Inui et al. [2019] pointed out that Martian ions with high speeds form a plume in the +E-hemisphere, while dense and slow-speed ions form an ion trail in the –E-hemisphere. Both simulations and observations show that crustal fields can twist the Martian magnetotail [Luhmann et al., 2015; DiBraccio et al., 2018; Xu et al., 2020]. To lower the possible effects of these fields on magnetospheric field structure, Dubinin et al. [2019, 2021] focused solely on the northern hemisphere to study the field structure of Martian induced magnetosphere; they found that the draping fields wrap the planet in the +E-hemisphere and then propagate toward the –E-hemisphere. By studying the projected distribution of magnetic field in the plane perpendicular to the Sun–Mars line, Chai et al. [2019] argued that a looping magnetic field also rotates around the Martian magnetotail.

Although these studies have revealed some characteristics of the magnetic field configuration of the Martian magnetosphere, the 3-D configuration of the field structure and its variations remains unclear. Hence, our goal is (1) to draw the global 3-D magnetic morphology of the Martian magnetosphere based on the magnetic field data collected by MAVEN over a period of 6 years (2014.10-2020.12), and (2) to investigate the possible impacts brought about by the IMF, solar wind pressure, and planet rotation. Overall, such a study would benefit our understanding of solar wind interaction with Mars.

2 Coordinates and Data Set

In this paper, we adopt magnetic field data measured by the Magnetometer (MAG) [Connerney et al., 2015] from 1 October 2014 to 31 December 2020. MAG measures the

magnetic field vectors at sample rates 32 Hz and 1 Hz. To minimize the noise and high-frequency fluctuations, we use the data of 1s resolution.

Two Cartesian coordinate systems are involved in this study. The first uses Mars-centered Solar Orbital (MSO) coordinates, where the X_{MSO} axis points from the center of Mars to the Sun, the Z_{MSO} axis points to the North Pole of Mars' orbital plane, and the Y_{MSO} axis completes the right-handed system. The second is the Mars Solar Electric coordinates (MSE), where X_{MSE} points antiparallel to the upstream solar wind flow, Y_{MSE} points along the cross-flow magnetic field component of the upstream IMF, and Z_{MSE} points along the direction of the convection electric field in the solar wind. Since the magnetic field configuration of the induced magnetosphere is guided by the IMF orientation, one has to study the 3-D magnetic field structure of the Martian magnetosphere in MSE.

To organize magnetic field data in MSE, we select orbits where pristine solar wind can be measured. Similar to procedures adopted by Liu et al. [2021], we first identify orbits with identifiable bow shock crossings according to the jump variation of their magnetic field strength, the ion energy spectrum of the Solar Wind Ion Analyzer (SWIA) [Halekas et al. 2013], and the electron energy spectrum of the Solar Wind Electron Analyzer (SWEA) [Mitchell et al. 2016]. Then, for each orbit, we took the average of upstream solar wind 30 minutes before (after) the inbound (outbound) bow shock crossing; the averaged solar wind velocity and IMF are denoted $\vec{V}_{\rm sw1}$ and $\vec{B}_1$ ($\vec{V}_{\rm sw2}$ and $\vec{B}_2$), respectively. Because the IMF is usually time-varied, we chose orbits during which the IMF was steady to construct MSE coordinates. This steady IMF is defined when the angle between $\vec{B}_1$ and $\vec{B}_2$ is less than 30°. Thus, for a steady IMF, we have $\vec{X}_{MSE}=-\frac{\vec{V}_{\rm sw1}+\vec{V}_{\rm sw2}}{|\vec{V}_{\rm sw1}+\vec{V}_{\rm sw2}|}$, $\vec{Y}_{MSE}=\frac{\vec{B}_{\perp 1}+\vec{B}_{\perp 2}}{|\vec{B}_{\perp 1}+\vec{B}_{\perp 2}|}$, and $\vec{Z}_{MSE}=\vec{X}_{MSE}\times\vec{Y}_{MSE}$. The subscript "$\perp$" represents the cross-flow component of the IMF, which can be calculated by subtracting the flow-aligned component, e.g., $\vec{B}_{\perp 1}=\vec{B}_1-(\vec{B}_1\cdot\vec{X}_{MSE})\vec{X}_{MSE}$. The direction of $\vec{Z}_{MSE}$ is also the same as that of the solar wind electric field (**E**). The Cartesian components of the magnetic field along the X-axis, Y-axis, and Z-axis in MSE are denoted as B_x, B_y, and B_z, respectively.

We found 4179 orbits in total that satisfy the conditions of a steady IMF; the measured magnetic field vectors in those orbits were transformed into MSE. To exclude the influence of crustal fields, we only kept magnetic field data points satisfying $|B_{obs}| \geq 10|B_{model}|$, where

146 $|B_{obs}|$ is the recorded magnetic field strength and $|B_{model}|$ is the magnetic field strength
147 predicted by a state-of-the-art crustal fields model [Gao et al., 2021]. These data points constitute
148 the data set we used in this study. For solar wind parameters corresponding to these orbits, we
149 averaged those parameters outside the bow shock: for example, the average IMF of one given
150 orbit is $IMF = \frac{\vec{B}_1 + \vec{B}_2}{2}$.

151 To avoid statistical bias, we checked the IMF distribution of our data set. Figures 1a–1c
152 shows histograms of the upstream average IMF for each orbit. Here, the IMF strength is mostly
153 smaller than 5 nT and peaks at ~2.5 nT (Figure 1a). The direction of IMF is characterized by its
154 cone and clock angle. The cone angle—the angle between the IMF and $+X_{MSO}$—has a unimodal
155 distribution and peaks at ~90° (Figure 1b). The clock angle—the angle between the projected
156 IMF and $+Z_{MSO}$ in the YZ_{MSO} plane (and which increases rotationally from $+Z_{MSO}$ toward
157 $+Y_{MSO}$)—exhibits a bimodal distribution with peaks reaching 90° and 270° (Figure 1c). The IMF
158 distributions in our data set are consistent with typical ones regarding the upstream solar wind
159 condition at Mars [Liu et al., 2021]. Thus, our data set is statistically significant enough to survey
160 the average magnetic structure of the Martian induced magnetosphere.

161 As shown in Figures 1d–1f, the spatial region around Mars ($-2 < X_{MSE} < 3$ R_m, $-3 < Y_{MSE} < 3$
162 R_m, $-3 < Z_{MSE} < 3$ R_m) is adequately accounted for by our data set. In the following sections, we
163 will study the magnetic field structure within this region (MSE coordinates are used unless
164 otherwise stated.).
165

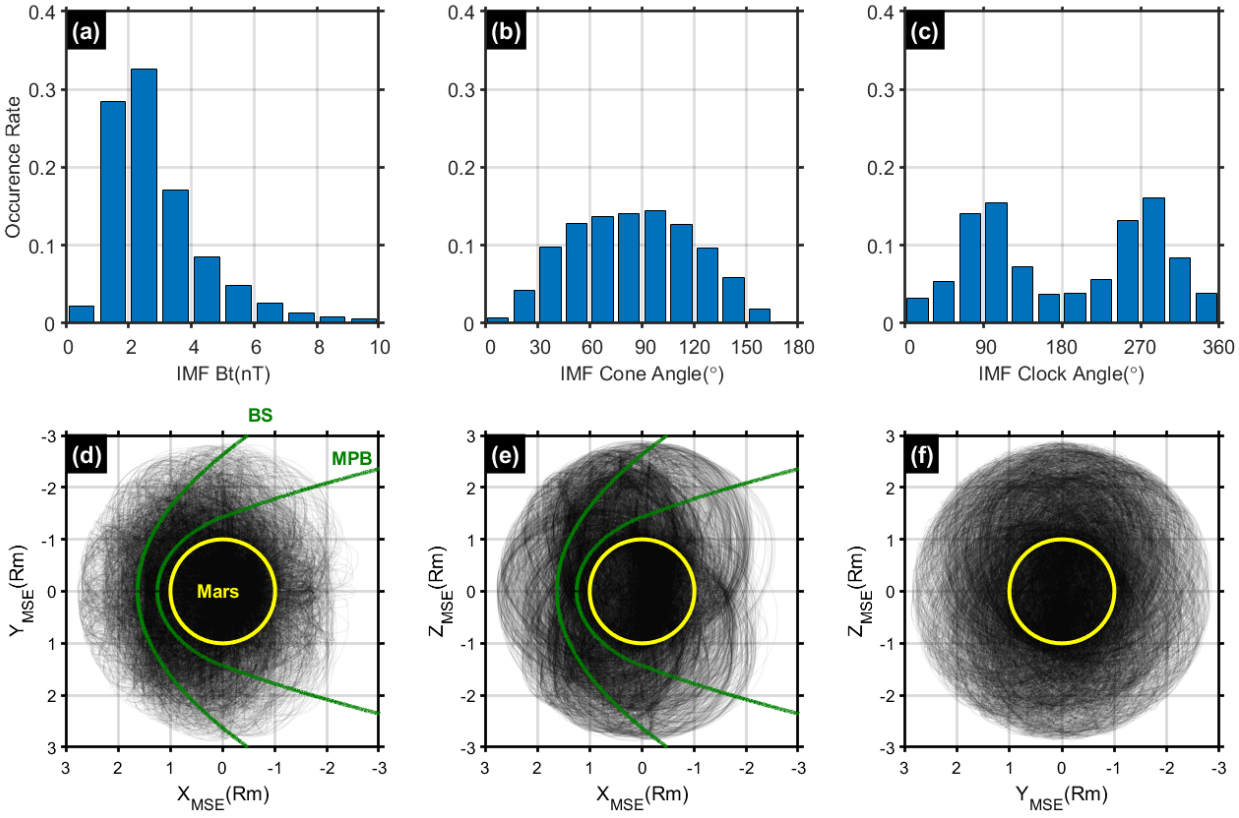

Figure 1. The upper panels show histograms of (a) the IMF strength, (b) the IMF clock angle, and (c) the IMF cone angle, respectively. The lower panels show orbit coverage of the data set, projected on the plane of (d) XY_{MSE}, (e) XZ_{MSE}, and (f) YZ_{MSE}, respectively. The yellow circles represent the body of Mars, while the green curves represent the nominal shape of the bow shock (BS) and the magnetic pile-up boundary (MPB) [Trotignon et al., 2006].

3 Statistical Results

To establish and draw the 3-D characteristics of the magnetic field configuration around Mars, we first check the average two-dimensional distributions of magnetic field vectors in the slices of the XZ_{MSE}, XY_{MSE}, and YZ_{MSE} planes, respectively, at different locations. Each slice is partitioned by a bin of 0.2×0.2 Rm, and the field vectors located in the slice are averaged for each bin. To ensure statistical significance, we ignore bins whose data points are fewer than ten.

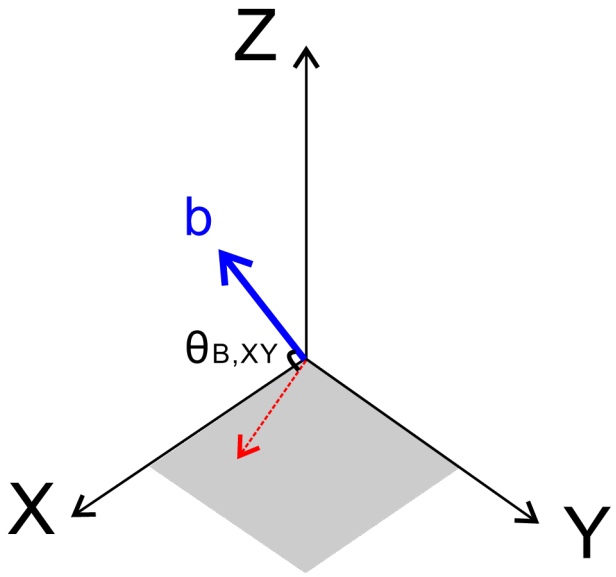

Figure 2. The sketched diagram to show the orientation of the unit magnetic field vector. The blue arrow represents the unit magnetic field vector ($\vec{b}$), the red arrow denotes the projection of $\vec{b}$ on XY_{MSE} plane. The $\theta_{B,XY}$ is the angle between $\vec{b}$ and XY_{MSE} plane.

To study the 3-D field structure, we also need to evaluate how much the average field vectors deviate from the slices above by calculating the angle between these vectors and the slices of XZ_{MSE}, XY_{MSE}, YZ_{MSE} planes, respectively:

$$\begin{cases} \theta_{B,XZ} = a\sin(b_y) \\ \theta_{B,XY} = a\sin(b_z) \\ \theta_{B,YZ} = a\sin(b_x) \end{cases} \quad (1)$$

where b_x, b_y, b_z represent the x, y, z component of the average unit magnetic field vector respectively in the bin. Taking $\theta_{B,XY}$ as an example (see Figure 2), the $\theta_{B,XY}$=90°(–90°) represents that the field lines are pointing along $+Z_{MSE}$ ($-Z_{MSE}$), while $\theta_{B,XY}$=0° represents the field lines are parallel to XY_{MSE} plane. Furthermore, a larger $\theta_{B,XY}$ indicates is the field lines are more perpendicular to the XY_{MSE} plane.

3.1 Magnetic Field Structure in XZ Plane

We first check the distribution of the magnetic field in different slices of XZ_{MSE} planes, with each slice having a thickness of 0.5 Rm within -2Rm $<Y_{MSE}<$ 2Rm. Based on the average distribution of the B_x, B_y, and B_z components in the bin of each slice, we can plot the average projected magnetic field lines (MFLs) in the XZ_{MSE} plane, while calculating the $\theta_{B,XZ}$ according to Eq. (1).

In Figure 3, the upper panels show field distributions for slices in the $+Y_{MSE}$-hemisphere (Figures 3a–3d), while the lower panels do so for slices in the $-Y_{MSE}$-hemisphere (Figures 3e-3h). As we can see, the MFLs are directed tailward (sunward) in the $+Y_{MSE}$ ($-Y_{MSE}$) –hemisphere, which means the IMF, pointing basically towards the $+Y_{MSE}$ direction, begins draping near the planet. Meanwhile, we notice that, from both flanks along Y_{MSE} to the central meridian, the draping MFLs outside the magnetic pile-up boundary tilt towards the nightside magnetic equatorial plane ($\sim Z_{MSE}= 0$); thus, the MFLs looks like they are "sinking" into the Martian wake. This pattern is reminiscent of the "sinking fields" observed in the Venusian magnetotail [Rong et al., 2014]. We also notice that the "sinking fields" from $+Z_{MSE}$ –hemisphere can extend down to $\sim Z_{MSE}= -1$ Rm; thus, "sinking fields" are more significant in the $+Z_{MSE}$–hemisphere than in the $-Z_{MSE}$–hemisphere, which is consistent with the hemispheric asymmetry of "sinking fields" reported by Rong et al. [2014] in the Venusian tail. Recent studies by Dubinin et al. [2019, 2021] have likewise reported the E-asymmetry of draping field structure in Martian tail.

Meanwhile, outside both flanks ($|Y_{MSE}|>1.5$ Rm; see Figures 3a and 3e), the "sinking" field lines from both ±E-hemispheres are basically symmetrical respective to the plane of $Z_{MSE}=0$, indicating that the E-asymmetry is weaker there.

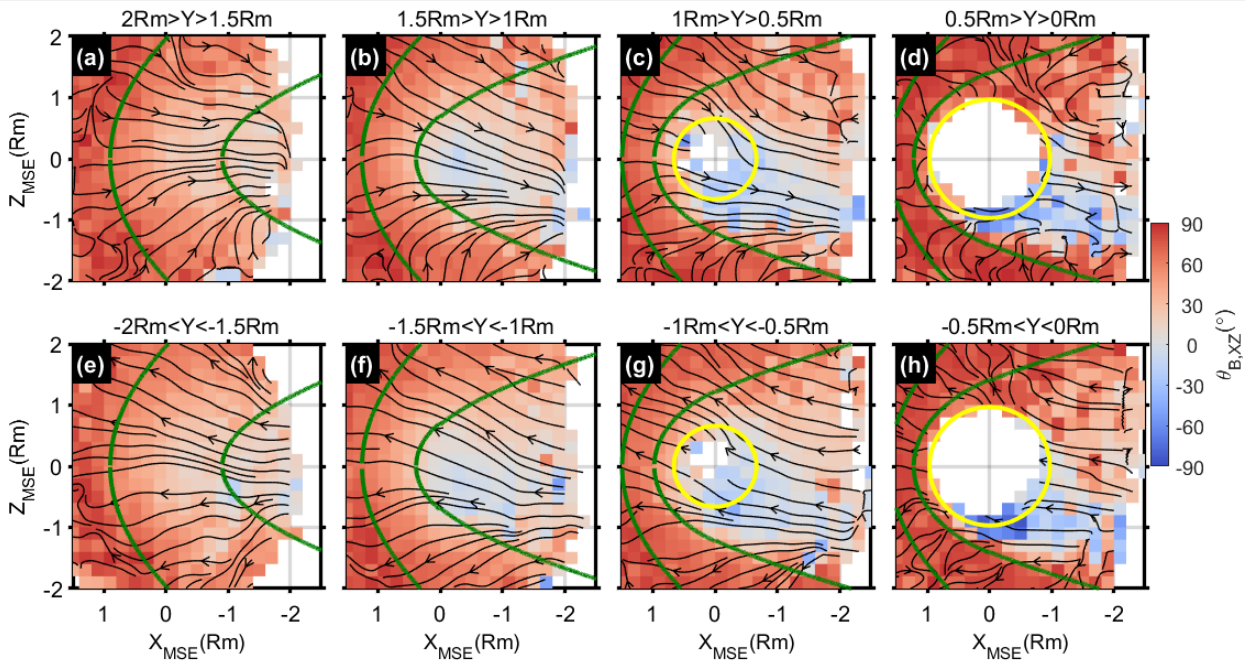

Figure 3. Average distributions of $\theta_{B,XZ}$ in the slices of the XZ_{MSE} plane within different ranges of the Y_{MSE} coordinate. Overplotted black lines with arrows denote the average MFLs. MFLs with red- (blue)-colored regions mean MFLs have a positive (negative) B_y component. In each panel or slice, the yellow circle represents the mean cut of Mars' body while the two green curves represent the mean cut of the nominal BS, MPB shape. Taking panel c as an example, the two green curves and the yellow circle are cuts of the BS, MPB shape and Mars' body, respectively, at Y_{MSE}=0.75 Rm.

Additionally, when approaching the central meridian from both flanks, the polarity of B_y component in some parts of the –E-hemisphere becomes negative (see negative $\theta_{B,XZ}$ in Figure 3); thus, corresponding MFLs seem stretched (Figures 3b–3c and Figures 3f–3g) and even "pinched" nearer the central meridian (Figures 3d-3h). Both "sinking" and "pinched" effects show that MFLs in the –E-hemisphere are tightly wrapped around the planet.

3.2 Magnetic Field Structure in XY Plane

Using the same procedures in subsection 3.1, we examine the magnetic field structure in slices of the XY_{MSE} plane.

Figure 4 shows distributions of $\theta_{B,XY}$ and the average MFLs in slices of the XY_{MSE} plane with a thickness of 0.5 Rm from Z_{MSE} = 2Rm to Z_{MSE} = –2Rm.

Clearly, each panel of Figure 4 shows an IMF that basically points towards $+Y_{MSE}$ in the upstream and bends upon approaching the planet. The bent MFLs are draped around the planet, which results in a positive Bx in the $–Y_{MSE}$-hemisphere and a negative Bx in the $+Y_{MSE}$-hemisphere. From the flanks of both ±E-hemispheres to the equator region (Z_{MSE} = 0), the draped MFLs are more tightly wrapped around the planet on the dayside and the field lines more stretched in the down tail.

Interestingly, the field lines in the wake of the –E-hemisphere are highly stretched and are even "pinched" towards the central meridian or plasma sheet (Figures 4f – 4h). The "pinched" field lines in the –E-hemisphere correspond to the negative B_y component, as noted in Figure 3.

It is important to note from Figure 4 that $\theta_{B,XY}$ in the +E-hemisphere is positive (negative) when $Y_{MSE}<0$ ($Y_{MSE}>0$), a feature that extends even to the –E-hemisphere (Figures 4g – 4h). In contrast, the opposite distribution pattern of $\theta_{B,XY}$ only occurs near the flank of –E-hemisphere (Figures 4e – 4f). The distribution of $\theta_{B,XY}$ demonstrates that the draped MFLs with $Z_{MSE}> –1$ Rm "sinks" towards the –E-direction, while the draped MFLs with $Z_{MSE}< -1$ Rm "sinks" towards the +E-direction. The E-asymmetry of these "sinking" field lines, as demonstrated by Figure 4, is consistent with our findings in Figure 3.

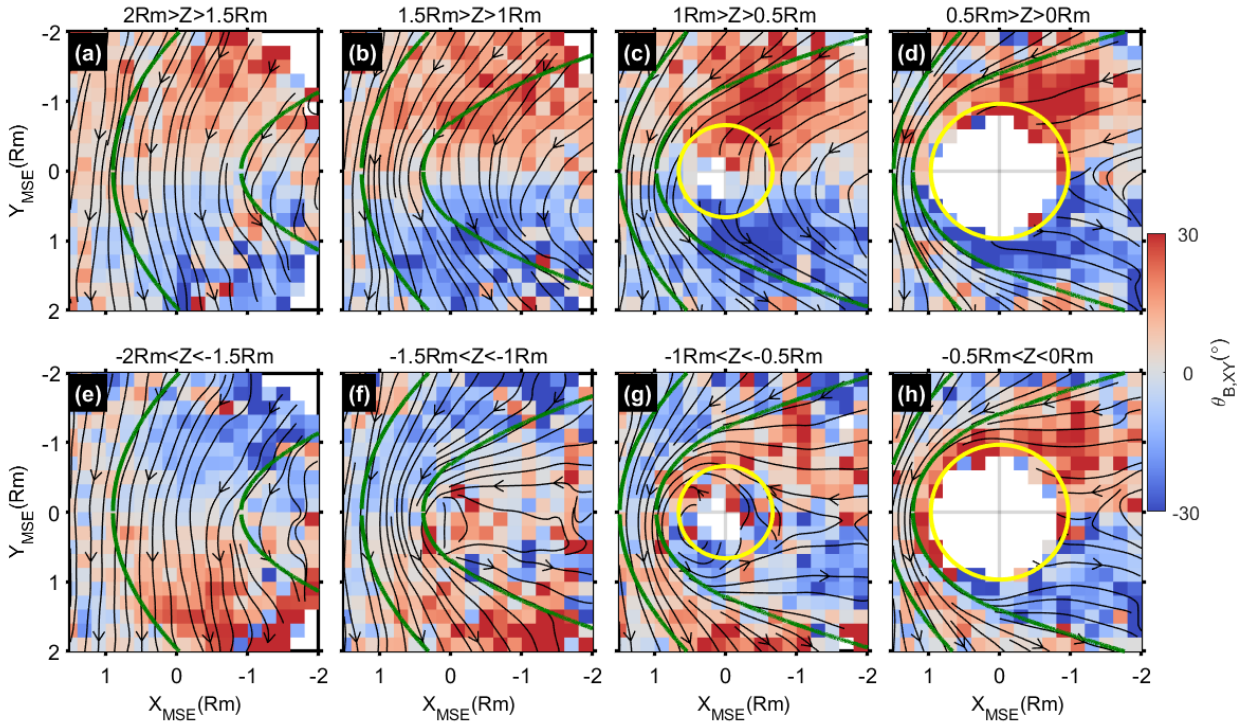

Figure 4. Average distributions of $\theta_{B,XY}$ in slices of the XY_{MSE} plane within different ranges of Z_{MSE} coordinates. Overplotted black lines with arrows denote the average MFLs. The format is the same as that of Figure 3.

3.3 Magnetic Field Structure in YZ Plane

Now we examine the magnetic field structure in slices of the YZ_{MSE} plane. Figure 5 shows distributions of $\theta_{B,YZ}$ and the average MFLs in slices of the YZ_{MSE} plane, with thickness 0.4 Rm, from dayside to nightside. Again, distributions of $\theta_{B,YZ}$ indicate that the magnetic field has a positive Bx component in the $-Y_{MSE}$-hemisphere and a negative Bx component in the $+Y_{MSE}$-hemisphere, which suggests that MFLs are bent with respect to Y_{MSE}=0 and are draped around the planet.

In the YZ_{MSE} plane, MFLs on the dayside point basically along $+Y_{MSE}$ direction (Figures 5a – 5b); nonetheless, as X_{MSE} moves downstream, the pattern of the MSLs becomes bulge-like when Z_{MSE} >–1 Rm and more concave-like when Z_{MSE} <–1 Rm (Figures 5c–5f). When we

consider the reversed polarity of the Bx component with respect to the plane Y_{MSE}=0, these bulge-like or concave-like patterns correspond to "sinking field" projections on the YZ_{MSE} plane.

It is interesting to note that the dominance of bulge-like MFLs around the planet (Z_{MSE} >-1 Rm) results in the appearance of the "loop field" as presented by Chai et al. [2019].

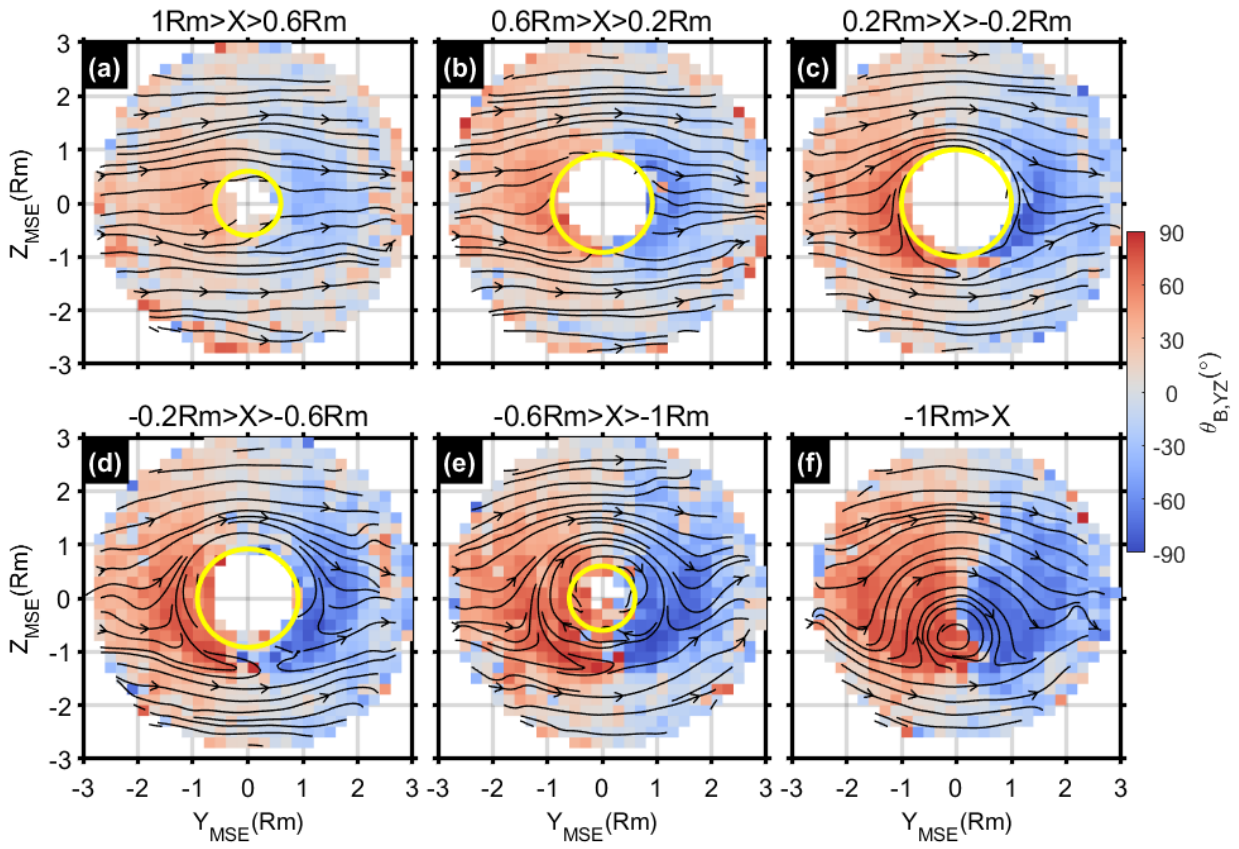

Figure 5. Average distributions of $\theta_{B,YZ}$ in slices of the YZ_{MSE} plane within different ranges of the X_{MSE} coordinate. Overplotted black lines with arrows denote average MFLs. The format is the same as that of Figure 3.

3.4 Visualization of 3-D MFLs

In the above subsections, we studied the projection of the magnetic field structure on different planes. Here, we draw the global 3-D magnetic field configuration directly by partitioning the spatial volume $X_{MSE}(-3\sim3R_M)$*$Y_{MSE}(-3\sim3R_M)$*$Z_{MSE}(-3\sim3R_M)$ by a bin of 0.2Rm

280 ×0.2Rm×0.2Rm and averaging the data points in each bin. Using these averaged data points,
281 we plot the 3-D configuration of MFLs around Mars in Figure 6.

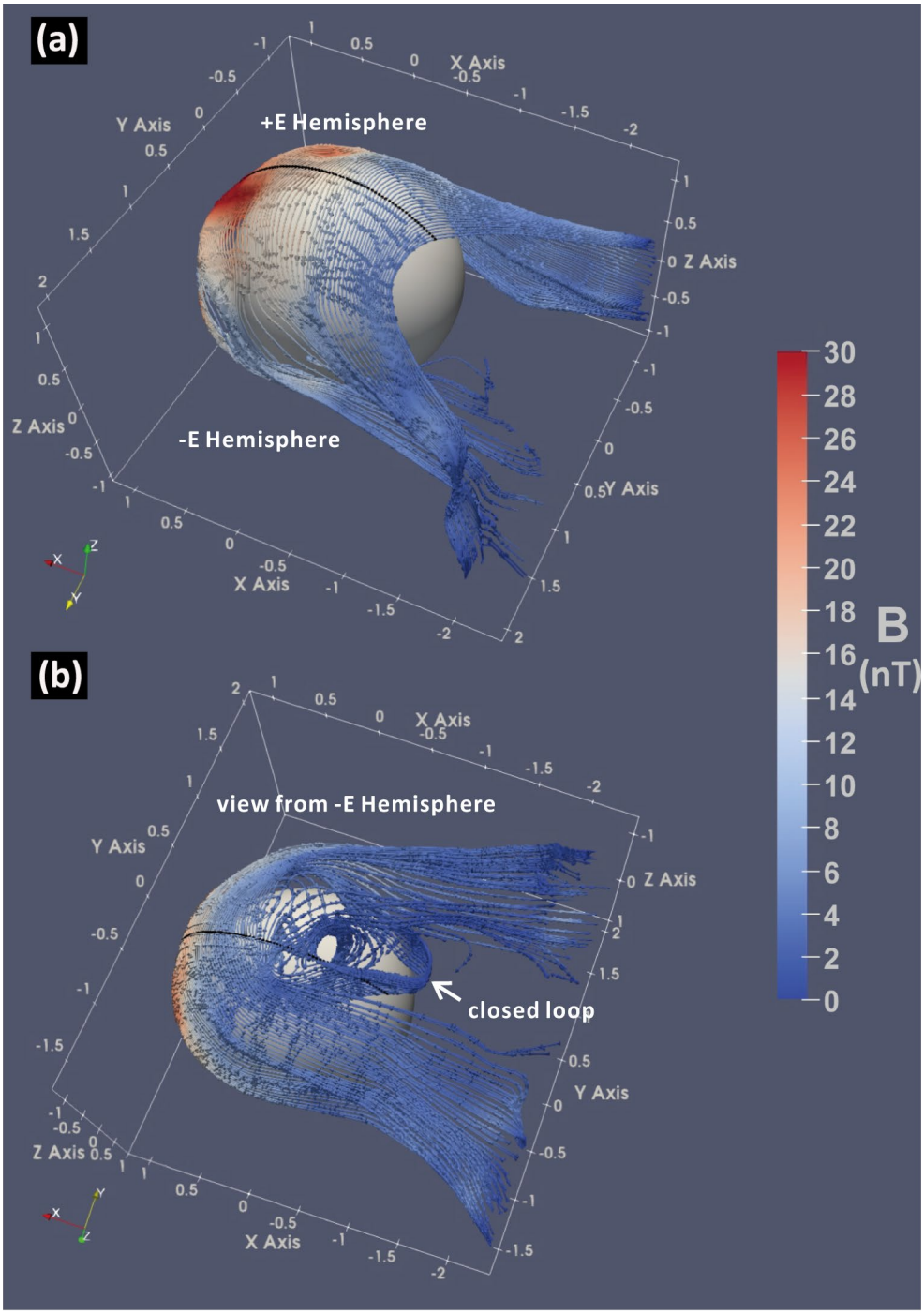

282

283 **Figure 6.** Average 3-D magnetic field lines in (a) the +E-hemisphere ($Z_{MSE}>0$) and (b) the E-
284 hemisphere ($Z_{MSE}<0$). MFLs are colored according to field strength. The black dots in the XZ_{MSE}
285 plane are the starting points for tracing the average MFLs, which are equally spaced within the
286 solar zenith angle range of 0°~135° with constant altitude of 0.2 Rm.

As shown in Figure 6a, the configuration of MFLs in the +E-hemisphere is largely consistent with the classical draping pattern: that is, the MFLs flare with respect to the plane of Y_{MSE}=0, and these flaring field lines, after slipping over the terminator, tilt towards the magnetic equatorial plane as "sinking" fields. Nonetheless, the draped MFLs near the magnetic equatorial plane do not flare significantly but are "pinched" towards the central meridian in the wake. In contrast to Figure 6a, the draped MFLs in the E-hemisphere are generally "pinched" towards the central meridian in the wake (Figure 6b). We notice, in particular, that a closed magnetic loop could form over the pole of –E-hemisphere, which is consistent with the picture shown in Figure 4g. This magnetic loop was also noticed in previous studies [Dubinin et al., 2019; 2021].

4. Average Structure of the Magnetotail Current Sheet

As mentioned above, there is an evident E-asymmetry of the draped field lines in the Martian wake, which may imply a similar E-asymmetry in the structure of the induced magnetotail current sheet. In this section, we attempt to quantitatively diagnose the averaged properties of Martian current sheet, which will enable us to interpret the plasma dynamics of current sheet.

To consider the orbit coverage of MAVEN while avoiding the influence of the magnetosheath (see Figure 1), we confine the studied tail region to $-1Rm<X_{MSE}<-2$ Rm and $|Y_{MSE}|<1.5Rm$, and show the distribution of Bx component in Figure 7a. It is clear from Figure 7a that a tail current sheet separating two lobes with an opposite polarity of the Bx component is located at $Y_{MSE}\sim0$. To survey the possible variations of the current sheet structure along the Z_{MSE}-axis, we study four regions of the magnetic field structure within Z_{MSE}-axis ranges: that is, $0.5\ Rm< Z_{MSE} <1Rm$, $0<Z_{MSE}<0.5Rm$, $-0.5\ Rm< Z_{MSE} <0$, and $-1Rm< Z_{MSE} <-0.5$ Rm (see black dashed regions in Figure 7a). We project the location of MPB at $X_{MSE}= -1Rm$ onto Figure 7a (see the green circle). Since the radius of MPB increases as it moves tailward, $X_{MSE}=-1Rm$ is the lowest limit of MPB in our studied region. It is apparent that these four regions are inside the MPB.

To estimate the magnetic field structure over the current sheet in each region, we have to check the profiles of the magnetic field over the current sheet. Because the Bx component and the Bz component are correlated in Martian magnetotail (see Figure 3), minimum variance

316 analysis (MVA) of the magnetic field in each region [Sonnerup & Scheible,1998] can help
317 remove such correlations. MVA yields three eigen values ($\lambda_1 \geq \lambda_2 \geq \lambda_3 > 0$) and their corresponding
318 eigenvectors $\{\vec{L}, \vec{M}, \vec{N}\}$. The three eigenvectors represent the directions of maximum,
319 intermediate, and minimum variance of the magnetic field. They are orthogonal and constitute a
320 local coordinate of the current sheet ($\vec{L} = \vec{M} \times \vec{N}$). $\vec{L}$ points along the magnetic field direction in
321 the lobe, $\vec{M}$ is basically along $\vec{E}_{SW}$ and tangential to the current sheet plane, and $\vec{N}$ is the
322 normal of current sheet and points basically along the Y_{MSE}-axis. The components of the average
323 magnetic field along $\vec{L}$, $\vec{M}$, and $\vec{N}$ are labelled B_L, B_M, and B_N.

324 The average profiles of B_L (black lines), B_M (green lines), and B_N (blue lines) against Y_{MSE}
325 for each region are shown in Figures 7b-7e. For all the regions, the B_M and B_N components are
326 basically constant, while B_L varies significantly over the current sheet (Y_{MSE}~0 plane), which
327 demonstrates that the field structure of the Martian tail current sheet is one-dimensional (1-D).
328 Because the yielded $\vec{L}$ for each region is well distinguished from $\vec{M}$ and $\vec{N}$, as demonstrated
329 by $\lambda_1 \gg \lambda_2, \lambda_3$, and the normal direction $\vec{N}$ is basically aligned with the Y_{MSE} axis (not shown
330 here), we could fit the profiles of B_L to a typical 1-D Harris sheet model: e.g.,
331 $B_L = B_0 \tanh(\frac{Y_{MSE} - y_0}{L})$ [Harris, 1962], where B_0 is the lobe field strength, L is the typical scale
332 of the sheet, and y_0 is the normal shift of the sheet center. Coefficients of the adjusted R-square
333 (>0.9) indicate that the fitting results are satisfactory (see Table 1).

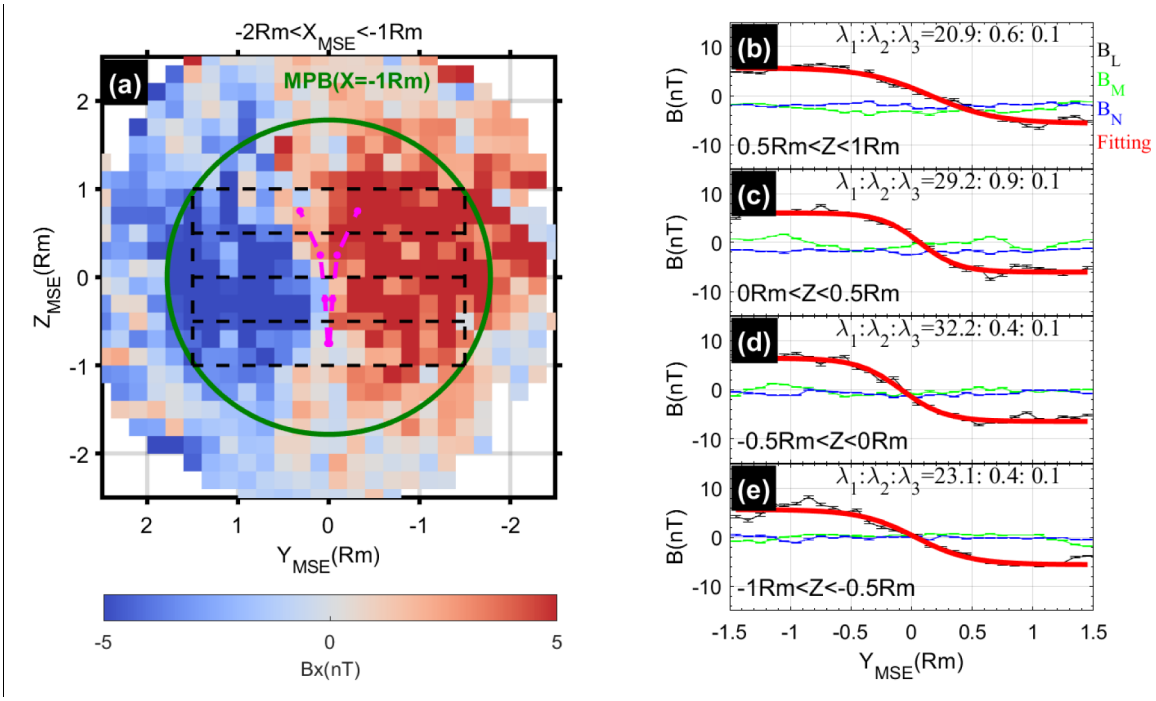

Figure 7. The left panel shows the distribution of Bx in the Martian magnetotail (–2Rm<X<-1Rm). The green cycle marks the nominal MPB shape when X=–1 Rm. The tail region is partitioned into four regions (rectangles marked by dashed lines, each with a width of 3Rm and a height of 0.5 Rm from Z_{MSE}=–1 Rm to Z_{MSE}=+1 Rm). The magenta dashed lines outline the thickness of the current sheet according to the curvature radius of the MFLs. The right panel shows the average profiles of B_L (black lines), B_M (green lines), and B_N (blue lines) against Y_{MSE} in each region. The lengths of the error bars are $2\times1.96\frac{\sigma}{\sqrt{n}}$, representing a 95% confidence interval, where $\frac{\sigma}{\sqrt{n}}$ is the standard error of the mean. The red dashed lines denote the fit curves of the Harris sheet model. The ratio of the three eigenvalues derived from MVA are labelled.

Based on the fitted parameters, the cross-tail current density at sheet center, which flows basically towards **E**, can be estimated as $J=\frac{B_0}{\mu_0 L}$, and the minimum curvature radius of MFLs reached at the sheet center can be estimated as $R_{c,\min}=\frac{<B_N>L}{B_0}$, if B_M is omitted, where $<B_N>$ is the average B_N component over the current sheet. $R_{c,\min}$ can be regarded to have half the thickness of the current sheet [e.g., Rong et al., 2014; Shen et al., 2007]. The resulting tailward Ampere force at the sheet center can be roughly estimated as $J\times B\sim J<B_N>$. Fitted parameters are listed in Table 1.

Table 1. Estimated Parameters of the Magnetotail Current Sheet in Different Regions

Region	B_0 (nT)	L (Rm)	R^2	<B_N> (nT)	R_{c_min} (Rm)	J (nA/m^2)	$\vec{J}\times\vec{B}$ (nT*nA/m^2)
0.5Rm<Z<1 Rm	5.67	0.54	0.97	3.35	0.32	2.48	–8.31
0 <Z<0.5Rm	6.05	0.32	0.98	1.78	0.09	4.47	–7.96
-0.5Rm <Z<0	6.42	0.36	0.98	0.75	0.04	4.23	–3.17
–1Rm <Z<–0.5Rm	5.62	0.45	0.95	–0.12	0.009	2.93	0.35

[a] R^2 is the coefficient of the adjusted R square, which indicates fitting goodness (closer to one means a better fit).
[b] <B_N> is the averaged value of B_N over the range –1.5Rm<Y_{MSE}<1.5Rm.
[c] R_{c_min} is the estimated magnetic field curvature radius at the center of current sheet.
[d] J is the estimated current density at the center of current sheet.
[e] This is the estimated force of J×B at the center of current sheet. The +/– sign means the direction of J×B is sunward/tailward.

From Table 1, the Martian magnetotail has an evident E-asymmetry: the current sheet in the +E-hemisphere has a larger B_N component, is thicker, and has a stronger tailward Ampere force, but in the – E-hemisphere the sheet has a smaller B_N component, is thinner, and has a weaker Ampere force. The polarities of B_N and $\vec{J}\times\vec{B}$ are even reversed in the region of –1Rm <Z<–0.5Rm. The E-asymmetry of $\vec{J}\times\vec{B}$ demonstrates that ampere force (which plays out as magnetic tension force) can accelerate plasma sheet ions moving tailward, so that tailward velocity is greater near the flank of +E-hemisphere. Considering the number density of ionospheric plasma ions ~1cm^{-3} (~5cm^{-3}) in +E (–E)-hemisphere [Inui et al., 2019], and the average of $\vec{J}\times\vec{B}$ is –8.31 nT*nA/m^2 (–3.17 nT*nA/m^2) in +E (–E) hemisphere, these ions could be accelerated to ~180eV (~15eV) within a distance of 1Rm in the +E (–E) hemisphere by $\vec{J}\times\vec{B}$ (the accelerated energy equals the product of $\vec{J}\times\vec{B}$ and distance). Thus, the ions in the current sheet can be accelerated to a faster speed in the +E-hemisphere than that in the –E-hemisphere, which is consistent with previous observations [Dubinin et al., 2019; Inui et al., 2019]. Furthermore, the sunward $\vec{J}\times\vec{B}$ near the flank of the –E-hemisphere might explain, to some extent, sunward ions that tend to occur in the –E-hemisphere [Harada et al., 2015]. Further studies are necessary to address this issue.

In contrast to E-asymmetry, the lobe field B_0 is basically constant (5~6 nT) in the whole magnetotail. Current density at the current sheet center is relatively higher near the magnetic equator (– 0.5 R_M<Z_{MSE} < 0.5 R_M) than the current density near both flanks (0.5 R_M<|Z_{MSE}|< 1

380 R_M), and the distribution pattern is consistent with a previous study (see Figure 3b of Ramstad et
381 al. [2020]).

382

383 **5. Influence of Solar Wind Conditions and Crustal Fields**

384 **5.1 Influence of IMF Bx**

385 Previous studies on the induced magnetosphere of Venus have demonstrated that the
386 polarity of IMF Bx could modulate the draping of IMF around the planet [e.g., McComas et al.,
387 1986; Rong et al., 2016; Delva et al., 2017]. As sketched in Figures 8a–8b, under the presence of
388 significant upstream IMF Bx component, a kink-like field structure named inverse polarity
389 reversal layer (IPRL) (which a spacecraft would record when crossing it) [Romanelli et al., 2015]
390 would appear at the boundary of an induced magnetosphere. This IPRL would disappear when
391 IMF Bx ~0 (Figure 8c). However, IPRL on Mars has been seldom reported. Here, we use our
392 data set to check the effect of IMF Bx on the induced magnetosphere of Mars.

393 Our data set, which we confined to $|Z_{MSE}|<1.5Rm$, is divided into three subdatasets or
394 conditions: (1) IMF Bx<0 (cone angle<60°), (2) IMF Bx>0 (cone angle>120°), and (3) IMF
395 Bx~0 (60°<cone angle<120°). We applied the procedure from Section 3 and plotted average
396 MFLs for each subdatasets respectively in Figures 8d – 8f. From the patterns of the average
397 MFLs, one can clearly see that the IPRL is located at the magnetospheric boundary of $+Y_{MSE}$-
398 hemisphere ($+Y_{MSE}$-hemisphere) under IMF +Bx (–Bx). In contrast, IPRL disappears when IMF
399 Bx is negligible (Figure 7f). Simulation demonstrates that the density of oxygen ion is enhanced
400 in IPRL [Jarvinen et al., 2010]. Given the kink-like structure of IPRL, we suggest that IPRL
401 would induce sunward $\vec{J} \times \vec{B}$ or magnetic tension, which might counterbalance the tailward
402 plasma flow to some extent and cause ion enhancement.

403 Previous studies suggest that IMF Bx could also shift the Venusian magnetotail current
404 sheet and bring hemispheric asymmetry to the lobe magnetic flux [McComas et al., 1986], but
405 this effect is questioned by Rong et al. [2016]. Based on a limited data point of MGS, Romanelli
406 et al. [2015] argued that IMF Bx could shift the Martian magnetotail current sheet. The effect of
407 IMF Bx on the Martian magnetotail lies will be addressed exclusively in another paper.

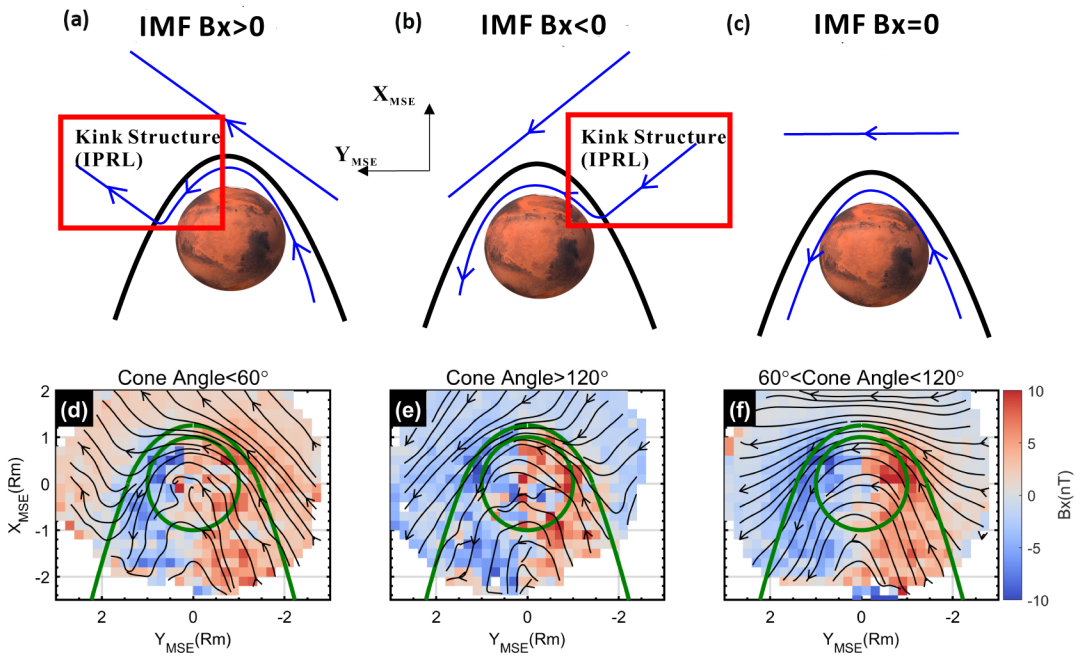

Figure 8. Draping configuration of magnetic field lines under (a) IMF +Bx, (b) IMF -Bx, and (c) IMF Bx~0. The distribution of Bx and MFLs under (d) IMF +Bx (cone angle<60°), (e) IMF -Bx (cone angle>120°), and (f) IMF Bx~0 (60°<cone angle<120°), respectively.

5.2 Influence of Solar Wind Dynamic Pressure

Solar wind dynamic pressure (Pdy) is believed to significantly impact the magnetic structure of an induced magnetosphere and ion escape [e.g. Ramstad et al., 2015; Dubinin et al., 2017; Nilsson et al., 2010, 2011; Zhang et al., 1994; Zhang et al., 2021]. Based on our dataset, we quantitatively evaluate how Pdy affects the magnetic field structure around Mars. To facilitate this, our dataset is dichotomized according to the median value of Pdy, i.e. 0.54 nPa. Data points with a Pdy higher than the median constitute a high Pdy subdataset, while those lower constitute a low Pdy subdataset. Comparing field distributions and configurations of these two subdatasets could highlight the effects of Pdy.

Distributions of magnetic field strength for the two subdatasets above demonstrate that magnetic fields around the planet, from the magnetosheath to the magnetic barrier as well as the whole magnetotail, are usually stronger during higher Pdy (Figures 9a–9b). This is plausible because draped MFLs are expected to be more compressed during higher Pdy.

In addition to the field strength, Pdy may also affect the flaring of the draped MFLs [Zhang et al., 1994]. Here, the flaring angle of MFLs, defined as $\theta_{B,X} = a\cos\left(\vec{b}\cdot\vec{x}\right)$, shows how much the magnetic field deviates from the x-axis. By surveying the response of $\theta_{B,X}$ to Pdy, we find that the magnetic field has a relatively smaller $\theta_{B,X}$ during higher Pdy than lower ones in the +E-hemisphere (Figure 9c). Thus, the draped MFLs in the +E-hemisphere generally stretch more or flare less during higher Pdy. The response of $\theta_{B,X}$ to Pdy in the –E-hemisphere, though less significant, is somewhat similar to that in the +E-hemisphere (Figure 9d). The reason seems obvious: MFLs with less flaring in the –E-hemisphere (see Figure 3) should be less sensitive to the impact of Pdy.

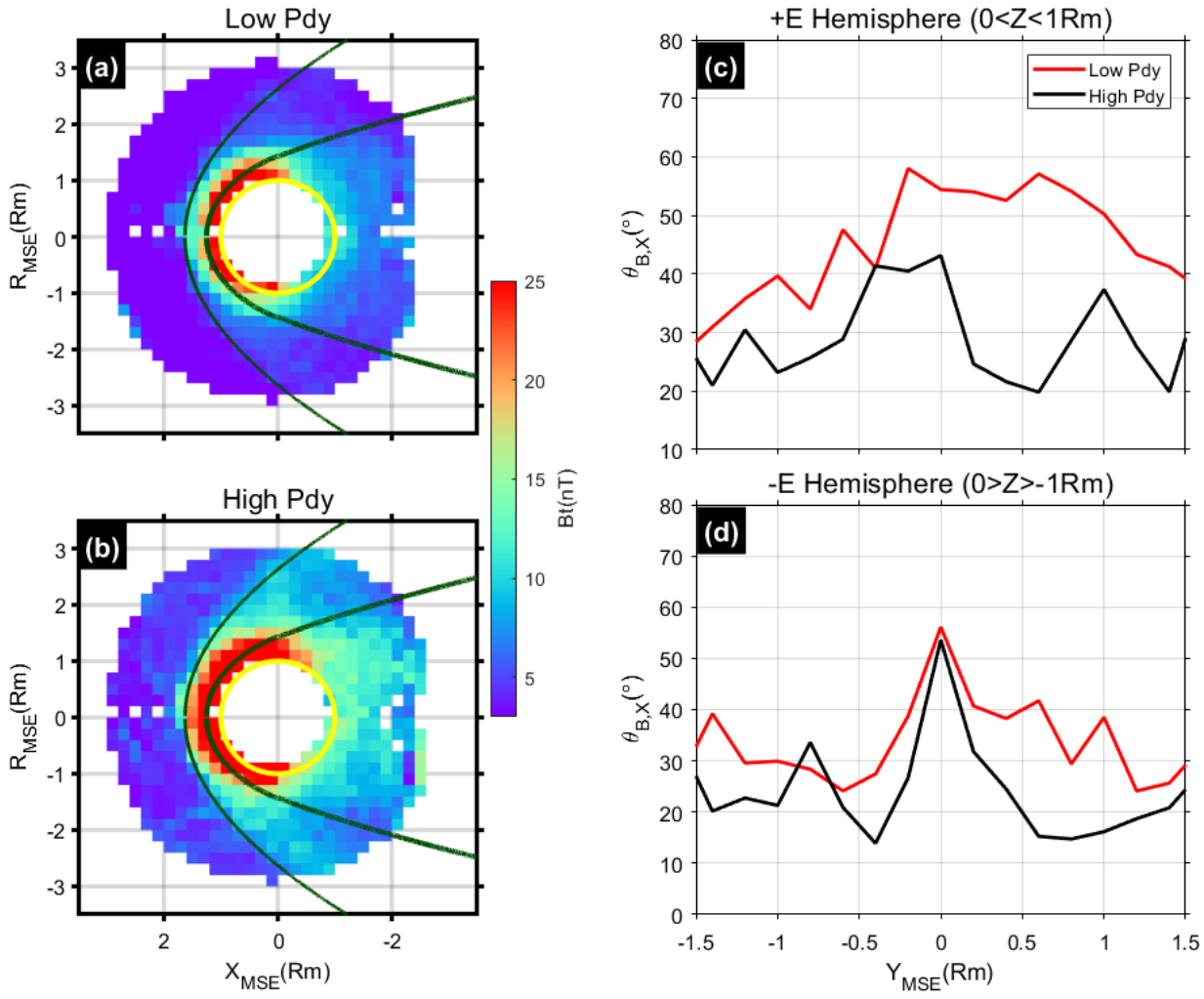

Figure 9. Response of the Martian induced magnetic field to dynamic pressure of solar wind. The left column shows the distributions of magnetic field strength during (a) lower Pdy and (b) higher Pdy. The Y coordinate is defined as $R_{MSE} = \mathrm{sign}(Z_{MSE}) * \sqrt{Y_{MSE}^2 + Z_{MSE}^2}$. The right column shows variations of the flaring angle $\theta_{B,XZ}$ against Y_{MSE} in (c) the +E-hemisphere and (d) the –E-hemisphere. Variation during during lower/higher Pdy is colored red/black.

5.3 Influence of Crustal Field Rotation

Previous studies suggested that the Martian magnetotail current sheet could be twisted by open field lines owing to the reconnection between the IMF and crustal fields [Luhmann et al., 2015; DiBraccio et al., 2018; Xu et al., 2020]; crustal fields may also influence the escape of Martian ions [e.g. Fang et al., 2010; Ramstad et al., 2016; Nilsson et al., 2011; Dubinin et al., 2020; Zhang et al., 2021]. Although the data points in our dataset are nearly unaffected by the crustal fields ($B_{model} < 0.1B_{obs}$), one cannot rule out their possible effects on the field structure of Martian magnetotail. Given Mars' rotation, the crustal field should diurnally modulate the tail field structure. Thus, in order to survey the effect of the crustal field, we check the response of the magnetic field distribution of Martian tail (–1Rm>X>–2Rm) to the planet's rotation.

To simplify the study, the dataset is divided into four subdatasets according to the local time (LT) when the strongest crustal fields are located at geo-longitude ~178° on the Martian surface (Figure 10a): (1) dawnside (3<LT<9), (2) dayside (9<LT<15), (3) duskside (15<LT<21), and (4) nightside (21<LT&LT<3). Because the IMF Bx component may shift the tail current sheet and bring about lobe asymmetry of magnetic flux [McComas et al.,1986], we only retain—to highlight possible effects brought about by planetary rotation—the data points with negligible IMF Bx (60°<cone angle<120°). Each of these data points has a corresponding LT of the strongest crustal fields, and the nearly uniform distribution of data points against these LTs rules out significant statistical bias among the four subdatasets (Figure 10b).

For these four subdatasets, we show distributions of Bx in the Martian tail when the strongest crustal field is located on the dawnside, the dayside, the duskside, and the nightside, respectively (Figures 10c–10f). Clearly, the distribution patterns of the subdatasets are similar;

all tail current sheets are roughly located at Y_{MSE} ~0. Thus, the rotation of crustal fields cannot significantly affect or modulate the configuration of the tail current sheet.

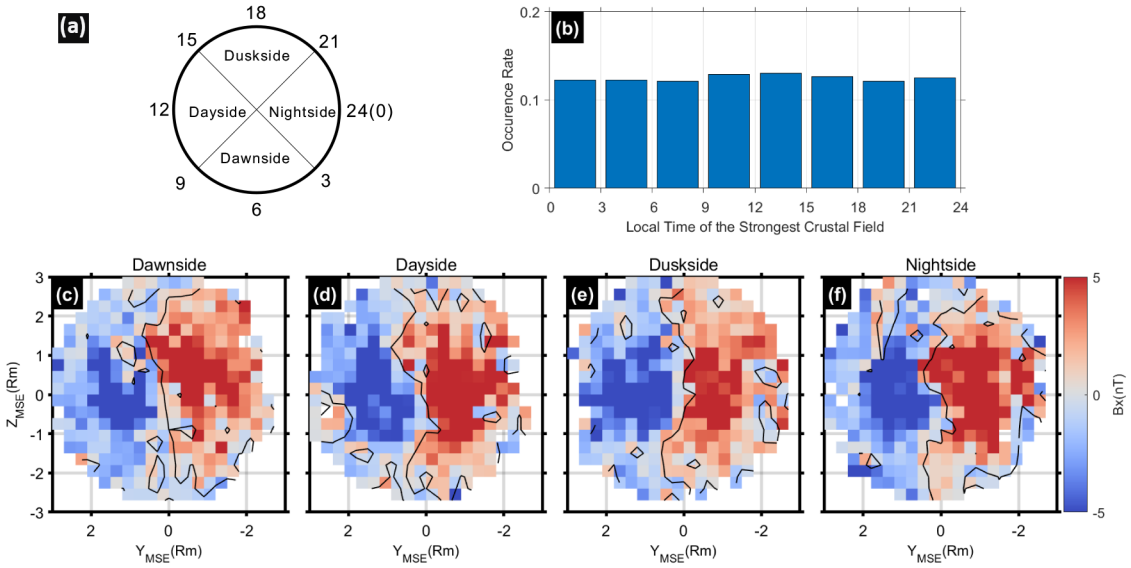

Figure 10. Effect of Martian rotation on tail field distribution. (a) Diagram of the four sectors chosen according to the local time of the strongest crustal field. (b) Distribution of data points against the local time of the strongest crustal field. The distribution of Bx in the YZ plane (-2<X<-1 Rm) when the strongest crustal field is on (c) the dawn side, (d) the day side, (e) the dusk side, and (f) the night side. Contours of Bx=0 are shown as black lines.

6 Discussion and Conclusion

In this study, which is based on a statistical survey of magnetometer measurements made by MAVEN from approximately 2014-10-01 to 2020-12-31, we derived the global 3-D magnetic field structure of the Martian induced magnetosphere. Our findings can be summarized as follows:

(1) The magnetic field structure around Mars is basically controlled by solar wind flow and IMF orientation, and the resulting morphology of the Martian magnetosphere conforms to the typical draping picture of an induced magnetosphere: a pair of tail lobes that is induced in the wake.

(2) The draped field lines from both flanks of the ±E-hemisphere are directed towards the magnetic equatorial plane, making the field lines look like they are "sinking" toward the wake. These "sinking" field lines could be driven by a downstream convergence of solar wind flow to the wake plasma cavity [Rong et al., 2014; Dubinin et al., 2019]. The field lines "sinking" from the +E-hemisphere are dominant in Martian tail because they can extend down to ~ Z_{MSE}= -1 Rm. The "sinking" field lines from the –E-hemisphere are more stretched and even "pinched" towards the central plasma sheet. The E-asymmetry of the "sinking fields" is consistent with previous studies on the field structure of Mars magnetotail [Dubinin et al., 2019, 2021] and also the Venusian magnetotail [Rong et al., 2014]. However, the E-asymmetry of "sinking fields" disappears outside the MPB, which indicates that asymmetry might arise due to the interaction of solar wind with the low-altitude atmosphere of Mars.

(3) The tail current sheet also shows an evident E-asymmetry corresponding to the E-asymmetry of draped field lines. The current sheet is thicker in the +E-hemisphere and thinner in the –E-hemisphere, and the tailward Ampere force $\vec{J} \times \vec{B}$ at the current sheet center, which is stronger near the flank of +E-hemisphere, is attenuated as it moves towards the –E-hemisphere. Thus, the tailward plasma flow can be accelerated to higher speeds by $\vec{J} \times \vec{B}$ near the flank of the +E-hemisphere. The much thinner current sheet and the sunward $\vec{J} \times \vec{B}$ at the flank of the –E-hemisphere may indicate that magnetic reconnection occurs preferentially there and explain the sunward ions observed there as well [Harada et al., 2015].

(4) Possible effects of IMF B_x, Pdy, and planetary rotation on the magnetic field structure are checked respectively. We find that a kink-like field structure appears at the boundary layer of the Martian magnetosphere under the presence of a significant IMF Bx component. While the global induced magnetic field around Mars is enhanced due to the compression of higher Pdy, the draped field lines in the tail flare less in such conditions. However, variations in the crustal field that are caused by planetary rotation do not seem to affect or modulate the configuration of tail current sheet significantly.

The E-asymmetry of the field structure has been observed in Venusian and Titan magnetotails [e. g. Saunders and Russell, 1986; Zhang et al., 2010; Du et al., 2013; Rong et al.,

2014; Chai et al., 2016; Simon et al., 2006]; thus, it appears to be a ubiquitous phenomenon of induced magnetospheres. However, the physical mechanism responsible for E-asymmetry is still unclear. Previous studies on Venus demonstrated that E-asymmetry of the B_y component has appeared at low altitude around the terminator [Du et al., 2013] and can extend to the distant tail [Saunders and Russell, 1986]. This asymmetry can be reproduced in hybrid and multifluid magnetfigureohydrodynamic simulations but not in single-fluid ones [e.g., Zhang et al., 2010; Du et al., 2013, and references therein; Jarvinen et al., 2013]. Thus, it seems that E-asymmetry could be associated with particle kinetic effects. Similar to research on Venus, our study on Mars also demonstrates that the appearance of the –By component starts at a low-altitude around the terminator of the –E-hemisphere (see Figures 2d and 2h). Recent observations by MAVEN showed that there is a trail of O^+, extended from nightside ionosphere, in the –E-hemisphere [Dubinin et al., 2019]. Thus, the interaction of the O^+ trail with the draped IMF would seem to result in a kinetic effect that "drags" the draped field lines, making them more stretched out, as well as resulting in a weaker B_y and signature of $–B_y$ in the hemisphere. Dubinin et al. [2019, 2021] suggested that ionospheric plasma is extracted and accelerates toward the +E direction by the pick-up effect of solar wind, which in turn produces an –E-directing recoil effect to the ionosphere, forming an ion trail in the –E hemisphere. However, this recoil force is not well identified. Additionally, it is also unclear why the appearance of $–B_y$ starts at a low-altitude around the terminator of the –E-hemisphere instead of the +E-hemisphere. It might be that the draped IMF penetrates more easily into the ionosphere when in the –E-hemisphere (as opposed to the +E-hemisphere) under the motional solar wind electric field, so that the signature of $–B_y$ tends to appear under those conditions. A combination of future simulations may help unravel the real mechanism of this E-asymmetry.

An important feature of E-asymmetry is a loop field structure over the pole of –E-hemisphere (Figure 6), which has been interpreted as the product of magnetic reconnection [Dubinin et al., 2019, 2021]. Given the explosive process of magnetic reconnection with a transient timescale, however, it is hard to believe that an average-yielded loop field structure, seen as a temporally static structure, is the product of magnetic reconnection. We suggest instead that the loop structure is induced by the inhomogeneous distribution of current density, and there should be stronger current density flowing $+Z_{MSE}$ direction embedded in the loop. The pattern of

the global Martian magnetospheric current derived by Ramstad et al. [2020] supports our interpretation.

Our study shows that the rotation of crustal field cannot affect the configuration of the tail current sheet significantly, which seems inconsistent with DiBraccio et al. [2018]. They argued that the current sheet could be twisted by open field lines owing to the reconnection between the IMF and crustal fields, a twist that could be more significant when the strongest crustal fields are on the noon. But the study by DiBraccio et al. was performed using MSO instead of MSE coordinates, which we favor here. We will address reasons for the discrepancy in a future study.

Finally, we also expect that future studies combining multipoint observations from China's TIANWEN-1 [Wan et al., 2020], MAVEN, and Mars Express [Barabash et al. 2006] might offer better opportunities to study the Martian magnetosphere and its response to solar wind variation and crustal field rotation.

Data Availability Statement

All MAVEN data used in this paper are available from NASA's Planetary Data System.
MAG data can be found at https://pds-ppi.igpp.ucla.edu/mission/MAVEN/MAVEN/MAG.
SWIA data can be found at https://pds-ppi.igpp.ucla.edu/mission/MAVEN/MAVEN/SWIA.
SWEA data can be found at https://pds-ppi.igpp.ucla.edu/mission/MAVEN/MAVEN/SWEA.

Acknowledgments

We would like to thank the entire MAVEN team and instrument leads for access to data and support. Special thanks to Jasper Halekas, David Mitchell and John E. P. Connerney for their contributions regarding the availability of SWIA, SWEA, and MAG data, respectively. This work is supported by the National Natural Science Foundation of China (Grant Nos. 41922031, 41774188), the Strategic Priority Research Program of Chinese Academy of Sciences (Grant No. XDA17010201), the Key Research Program of Chinese Academy of Sciences (Grant No. ZDBS-SSW-TLC00103), and the Key Research Program of the Institute of Geology & Geophysics, CAS (Grant No. IGGCAS- 201904, IGGCAS- 202102). Chi Zhang is supported by the China Scholarship Council (Student No. 202104910297). We also thank Jun Zhong and Chongjing Yuan for helpful suggestions, and Fang Qian for her encouragement.

References

Acuña, M. H., Connerney, J. E. P., Ness, N. F., Lin, R. P., Mitchell, D., Carlson, C.W., et al. (1999). Global distribution of crustal magnetism discovered by Mars Global Surveyor MAG/ER experiment. Science, 284, 790–793. https://doi.org/10.1126/science.284.5415.790

Acuña, M.H., et al., 1998. Magnetic field and plasma observations at Mars: initial results of the Mars Global Surveyor mission. Science,279, 1676–1680.

Barabash, S., et al. (2006), The Analyzer of Space Plasma and Energetic Atoms (ASPERA-3) for the Mars Express mission, Space Sci. Rev., 126, 113.

Barabash, S., Fedorov, A., Lundin, R., & Sauvaud, J.-A. (2007). Martian Atmospheric Erosion Rates. Science, 315(5811), 501–503.

Chai, L., Wan, W., Wei, Y., Zhang, T., Exner, W., Fraenz, M., ... & Zhong, J. (2019). The induced global looping magnetic field on Mars. The Astrophysical Journal Letters, 871(2), L27.

Chai, L., Wei, Y., Wan, W., Zhang, T., Rong, Z., Fraenz, M., ... & Barabash, S. (2016). An induced global magnetic field looping around the magnetotail of Venus. Journal of Geophysical Research: Space Physics, 121(1), 688-698.

Connerney, J. E. P., Acuña, M. H., Ness, N. F., Kletetschka, G., Mitchell, D. L., Lin, R. P., & Rème, H. (2005). Tectonic implications of Mars crustal magnetism. Proceedings of the National Academy of Sciences of the United States of America, 102(42), 14970 – 14975. https://doi. org/10.1073/pnas.0507469102

Connerney, J., Espley, J., Lawton, P., Murphy, S., Odom, J., Oliversen, R., & Sheppard, D. (2015). The MAVEN magnetic field investigation. Space Science Reviews, 195, 257–291.

Delva, M., Volwerk, M., Jarvinen, R., & Bertucci, C. (2017). Asymmetries in the magnetosheath field draping on Venus' nightside. Journal of Geophysical Research: Space Physics, 122(10), 10-396.

DiBraccio, G. A., Luhmann, J. G., Curry, S. M., Espley, J. R., Xu, S., Mitchell, D. L., et al. (2018). The twisted configuration of the Martian magnetotail: MAVEN observations. Geophysical Research Letters, 45, 4559–4568. https://doi.org/10.1029/2018GL077251

Du, J., C.Wang, T. L. Zhang, and E. Kallio (2013), Asymmetries of the magnetic field line draping shape around Venus, J. Geophys. Res. Space Physics, 118, 6915–6920, doi:10.1002/2013JA019127

Dubinin, E., & Fraenz,M. (2015).Magnetotails ofMars and Venus. In A. Keiling, C. M. Jackman, & P. A. Delamere (Eds.), Magnetotails in the solar system (pp. 43–59). Hoboken, NJ: John Wiley. https://doi.org/10.1002/9781118842324.ch3

Dubinin, E., Fraenz, M., Fedorov, A., Lundin, R., Edberg, N., Duru, F., & Vaisberg, O. (2011). Ion Energization and Escape on Mars and Venus. Space Science Reviews, 162(1), 173–211.

Dubinin, E., Fraenz, M., Pätzold, M., McFadden, J., Halekas, J., DiBraccio, G., et al. (2017). The effect of solar wind variations on the escape of oxygen ions from Mars through different channels: MAVEN observations. Journal of Geophysical Research: Space Physics, 122, 11,285–11,301. https://doi.org/10.1002/2017JA024741

Dubinin, E., Fränz, M., Modolo, R., Pätzold, M., Tellmann, S., Vaisberg, O., ... & Espley, J. (2021). Induced magnetic fields and plasma motions in the inner part of the Martian magnetosphere. Journal of Geophysical Research: Space Physics, 126(12), e2021JA029542.

Dubinin, E., Fränz, M., Pätzold, M., Woch, J., McFadden, J., Fan, K., ... & Zelenyi, L. (2020). Impact of Martian crustal magnetic field on the ion escape. Journal of Geophysical Research: Space Physics, 125(10), e2020JA028010.

Dubinin, E., Modolo, R., Fraenz, M., Päetzold, M., Woch, J., Chai, L., … DiBraccio, G. (2019). The induced magnetosphere of Mars. Asymmetrical topology of the magnetic field lines. Geophysical Research Letters, 46(22), 12722–12730.

Fang, X., Liemohn, M. W., Nagy, A. F., Luhmann, J. G., & Ma, Y. (2010). Escape probability of Martian atmospheric ions: Controlling effects of the electromagnetic fields. Journal of Geophysical Research: Space Physics, 115(A4).

Fang, X., Liemohn, M. W., Nagy, A. F., Luhmann, J. G., & Ma, Y. (2010). On the effect of the Martian crustal magnetic field on atmospheric erosion. Icarus, 206(1), 130-138.

Fedorov, A., Budnik, E., Sauvaud, J. A., Mazelle, C., Barabash, S., Lundin, R., … Yamauchi, M. (2006). Structure of the martian wake. Icarus, 182(2), 329–336.

Futaana, Y. , Wieser, G. S. , Barabash, S. , & Luhmann, J. G. . (2017). Solar wind interaction and impact on the venus atmosphere. Space Science Reviews.

Gao, J.W., Rong, Z.J., Klinger Lucy, Li, X.Z., Liu, D., Wei, Y. (2021). A spherical harmonic Martian crustal magnetic field model combining data sets of MAVEN and MGS, Earth and Space Science, doi: 10.1029/2021EA001860.

Halekas, J. S., D. A. Brain, R. J. Lillis, M. O. Fillingim, D. L. Mitchell, and R. P. Lin (2006), Current sheets at low altitudes in the Martian magnetotail, Geophys. Res. Lett., 33, L13101, doi:10.1029/2006GL026229.

Halekas, J. S., E. R. Taylor, G. Dalton, G. Johnson, D. W. Curtis, J. P. McFadden, D. L. Mitchell, R. P. Lin, and B. M. Jakosky (2013), The solar wind ion analyzer for MAVEN, Space Sci. Rev., doi:10.1007/s11214-013-0029-z.

Harada, Y., Halekas, J. S., McFadden, J. P., Mitchell, D. L., Mazelle, C., Connerney, J. E. P., ... & Jakosky, B. M. (2015). Marsward and tailward ions in the near‐Mars magnetotail: MAVEN observations. Geophysical Research Letters, 42(21), 8925-8932.

Harris, E. G. (1962), On a plasma sheet separating regions of oppositely directed magnetic field, Nuovo Cimento, 23, 115–121, doi:10.1007/BF02733547.

Inui, S., Seki, K., Sakai, S., Brain, D. A., Hara, T., McFadden, J. P., et al. (2019). Statistical study of heavy ion outflows from Mars observed in the Martian‐induced magnetotail by MAVEN. Journal of Geophysical Research: Space Physics, 124, 5482–5497. https://doi.org/10.1029/ 2018JA026452

Jakosky, B. M., et al. (2015), The Mars Atmosphere and Volatile Evolution (MAVEN) mission, Space Sci. Rev., doi:10.1007/s11214-015-0139-x.

Jarvinen, R., E. Kallio, and S. Dyadechkin (2013), Hemispheric asymmetries of the Venus plasma environment, J. Geophys. Res. Space Physics,118, 4551–4563, doi:10.1002/jgra.50387.

Jarvinen, R., Kallio, E., Dyadechkin, S., Janhunen, P., & Sillanpää, I. (2010). Widely different characteristics of oxygen and hydrogen ion escape from Venus. Geophysical research letters, 37(16).

Liu, D., Rong, Z., Gao, J., He, J., Klinger, L., Dunlop, M. W., ... & Wei, Y. (2021). Statistical Properties of Solar Wind Upstream of Mars: MAVEN Observations. The Astrophysical Journal, 911(2), 113.

Luhmann, J. G., Dong, C., Ma, Y., Curry, S. M., Mitchell, D., Espley, J., ... & Mazelle, C. (2015). Implications of MAVEN Mars near-wake measurements and models. Geophysical Research Letters, 42(21), 9087-9094.

Luhmann, J. G., S. A. Ledvina, and C. T. Russell (2004), Induced magnetospheres, Adv. Space Res., 33, 1905–1912.

Lundin, R. (2011). Ion acceleration and outflow from Mars and Venus: An overview. The plasma environment of Venus, Mars, and Titan, 309-334.

Ma, Y., Nagy, A. F., Hansen, K. C., DeZeeuw, D. L., Gombosi, T. I., & Powell, K. (2002). Three-dimensional multispecies MHD studies of the solar wind interaction with Mars in the presence of crustal fields. Journal of Geophysical Research, 107(A10), 1282–1289.

McComas, D. J., H. E. Spence, C. T. Russell, and M. A. Saunders (1986), The average magnetic field draping and consistent plasma properties in the Venus magnetotail, J. Geophys. Res., 91, 7939–7953, doi:10.1029/JA091iA07p07939.

Mitchell, D., Mazelle, C., Sauvaud, J.-A., Thocaven, J.-J., Rouzaud, J., Fedorov, A., et al. (2016). The MAVEN solar wind electron analyzer. Space Science Reviews, 200(1-4), 495–528.

Nilsson, H., Carlsson, E., Brain, D. A., Yamauchi, M., Holmström, M., Barabash, S., ... & Futaana, Y. (2010). Ion escape from Mars as a function of solar wind conditions: A statistical study. Icarus, 206(1), 40-49.

Nilsson, H., Edberg, N. J. T., Stenberg, G., Barabash, S., Holmström, M., Futaana, Y., … Fedorov, A. (2011). Heavy ion escape from Mars, influence from solar wind conditions and crustal magnetic fields. Icarus, 215(2), 475–484.

Nilsson, H., Zhang, Q., Wieser, G. S., Holmström, M., Barabash, S., Futaana, Y., … Wieser, M. (2021). Solar cycle variation of ion escape from Mars. Icarus, 114610.

Ramstad, R., Barabash, S., Futaana, Y., Nilsson, H., & Holmström, M. (2016). Effects of the crustal magnetic fields on the Martian atmospheric ion escape rate. Geophysical Research Letters, 43(20), 10-574.

Ramstad, R., Barabash, S., Futaana, Y., Nilsson, H., Wang, X. D., & Holmström, M. (2015). The Martian atmospheric ion escape rate dependence on solar wind and solar EUV conditions: 1. Seven years of Mars Express observations. Journal of Geophysical Research: Planets, 120(7), 1298-1309.

Ramstad, R., Brain, D. A., Dong, Y., Espley, J., Halekas, J., & Jakosky, B. (2020). The global current systems of the Martian induced magnetosphere. Nature Astronomy, 4(10), 979-985.

Romanelli, N., Bertucci, C., Gómez, D., & Mazelle, C. (2015). Dependence of the location of the Martian magnetic lobes on the interplanetary magnetic field direction: Observations from Mars Global Surveyor. Journal of Geophysical Research: Space Physics, 120(9), 7737-7747.

Rong, Z. J., G. Stenberg, Y. Wei, L. H. Chai, Y. Futaana, S. Barabash, W. X. Wan, and C. Shen (2016), Is the flow-aligned component of IMF really able to impact the magnetic field structure of Venusian magnetotail? J. Geophys. Res. Space Physics, 121, 10,978–10,993, doi:10.1002/2016JA022413.

Rong, Z. J., S. Barabash, Y. Futaana, G. Stenberg, T. L. Zhang,W. X. Wan, Y. Wei, X.-D. Wang, L. H. Chai, and J. Zhong (2014), Morphology of magnetic field in near-Venus magnetotail: Venus express observations, J. Geophys. Res. Space Physics, 119, 8838–8847, doi:10.1002/2014JA020461.

Saunders, M. A., and C. T. Russell (1986), Average dimension and magnetic structure of the distant Venus magnetotail, J. Geophys. Res., 91, 5589 – 5604, doi:10.1029/JA091iA05p05589.

Shen, C., X. Li,M. Dunlop, Q. Q. Shi, Z. X. Liu, E. Lucek, and Z. Q. Chen (2007), Magnetic field rotation analysis and the applications, J. Geophys. Res., 112, A06211, doi:10.1029/2005JA011584.

Simon, S. , Boesswetter, A. , Bagdonat, T. , Motschmann, U. , & Glassmeier, K. H. . (2006). Plasma environment of titan: a 3-d hybrid simulation study. Annales Geophysicae, 24(2006), 1113-1135.

Sonnerup, B. U. Ö., & Scheible, M. (1998). Minimum and maximum variance analysis. In G. Paschmann, & P. W. Daly (Eds.), chap. 8, *Analysis Methods for Multi‐Spacecraft Data, ISSI Sci. Rep. no. SR‐001* (pp. 185–220). Noordwijk, Netherlands: European Space Agency.

Titov, D. V., Svedhem, H., Koschny, D., Hoofs, R., Barabash, S., Bertaux, J. L., ... & Clochet, A. (2006). Venus Express science planning. Planetary and Space Science, 54(13-14), 1279-1297.

Trotignon, J. G., Mazelle, C., Bertucci, C., & Acuña, M. H. (2006). Martian shock and magnetic pile-up boundary positions and shapes determined from the Phobos 2 and Mars Global Surveyor data sets. Planetary and Space Science, 54(4), 357–369.

Wan, W., Wang, C., Li, C., Wei, Y., & Liu, J. (2020). The payloads of planetary physics research onboard China's First Mars Mission (Tianwen-1). Earth and Planetary Physics, 4(4), 331–332.

Xu, S., Mitchell, D. L., Weber, T., Brain, D. A., Luhmann, J. G., Dong, C., et al. (2020). Characterizing Mars's magnetotail topology with respect to the upstream interplanetary magnetic fields. Journal of Geophysical Research: Space Physics, 125, e2019JA027755. https://doi.org/10.1029/2019JA027755

Yeroshenko, Y., Riedler, W., Schwingenschuh, K., Luhmann, J. G., Ong, M., & Russell, C. T. (1990). The magnetotail of Mars: Phobos observation. Geophysical Research Letters, 17, 885–888. https://doi.org/10.1029/GL017i006p00885

Zhang, C., Rong, Z. J., et al. (2021). MAVEN Observations of Periodic Low-altitude Plasma Clouds at Mars. The Astrophysical Journal Letters, 922, L33. https://doi.org/10.3847/2041-8213/ac3a7d

Zhang, T. L., Schwingenschuh, K., Russell, C. T., Luhmann, J. G., Rosenbauer, H., Verigin, M. I., & Kotova, G. (1994). The flaring of the Martian magnetotail observed by the Phobos 2 spacecraft. Geophysical research letters, 21(12), 1121-1124.

Zhang, T., Baumjohann, W., Du, J., Nakamura, R., Jarvinen, R., Kallio, E., et al. (2010). Hemispheric asymmetry of the magnetic field wrapping pattern in the Venusian magnetotail. Geophysical Research Letters, 37, L14202, https://doi.org/10.1029/2010GL044020.